Estimating the graphite electrode phase evolution from electrode potential measurements

Materials & Design 266 (2026) 116218

Contents lists available at ScienceDirect

Materials & Design

journal homepage: www.elsevier.com/locate/matdes

Estimating the graphite electrode phase evolution from electrode potential measurements

Isac Borghed*, Xiaolei Bian, Yicun Huang[1], Torsten Wik*

Department of Electrical Engineering, Chalmers University of Technology, Hörsalsvägen 11, Gothenburg 412 96, Sweden

HIGHLIGHTS

- ICA knee-points reliably map to graphite phase transitions at low currents.
- Kernel smoothing bridges low- and higher-current phase estimations.
- The kernel standard deviation indicates the degree of lithiation inhomogeneity.
- A first step towards BMS-compatible alternatives to XRD-based phase-tracking.

ARTICLE INFO

Keywords:
Li-ion batteries
Graphite anode
Incremental capacity analysis
Kernel smoothing
Phase evolution

ABSTRACT

Knowledge of the internal state of lithium-ion batteries is crucial for the development of safe charging control algorithms. Most commonly, graphite is used as the negative electrode, possessing a high specific capacity and cycling stability. When such lithium-ion batteries are charged, lithium intercalates into the layered carbon structure, and the electrode material transitions through a series of phases differentiated by the number of carbon layers between each lithium layer. Each phase has different electrochemical properties, making it interesting to accurately track the phase content during lithiation. However, this quantity can only be measured through spectroscopic experiments, which cannot be included in any battery application. In this work, a method based on incremental capacity analysis and kernel smoothing is introduced to estimate the phase content of graphite electrodes from the electrode potential during constant-current charging. This kernel density function (KDF) method is validated at low currents using physics-based simulations of multiphase electrode dynamics, achieving an average phase estimation error below one percentage point per phase. Furthermore, we apply the KDF-method to experimentally measured coin cell data, for which the estimated phase content closely agrees with simulations in the mid to high range state of charge.

1. Introduction

The first commercially available lithium-ion battery (LIB) was released in 1991, and LIBs now play an important role in several technologies that are critical for the transition to a carbon neutral society, such as stationary energy storage and electric vehicles [1]. One remaining barrier to the widespread adoption of electric vehicles is their longer charging time compared with the refueling time of combustion vehicles [2]. However, simply increasing the charging rate (C-rate) can be detrimental to the battery health due to the many complex, interconnected degradation mechanisms present in LIBs [2–4].

An especially critical degradation process is lithium plating [3–5], where lithium is deposited on the graphite electrode instead of intercalating into it, leading to rapid capacity loss and an increased risk of thermal runaway. Under normal charging conditions, the plating reaction is not thermodynamically favorable compared to intercalation, but it can occur if the intercalation overpotential becomes negative with respect to lithium metal. This happens when the local surface concentration of the electrode particles reaches a maximum, meaning that no interstitial sites are available for further lithium intercalation. Such conditions can arise due to high current, low operating temperature, cell defects, and aging [3,5].

* Corresponding authors.
Email addresses: isacbo@chalmers.se (I. Borghed), tw@chalmers.se (T. Wik).
[1] Present address: Department of Information Technology, Uppsala University, Uppsala 751 05, Sweden.

https://doi.org/10.1016/j.matdes.2026.116218
Received 23 February 2026; Received in revised form 7 May 2026; Accepted 11 May 2026
Available online 12 May 2026

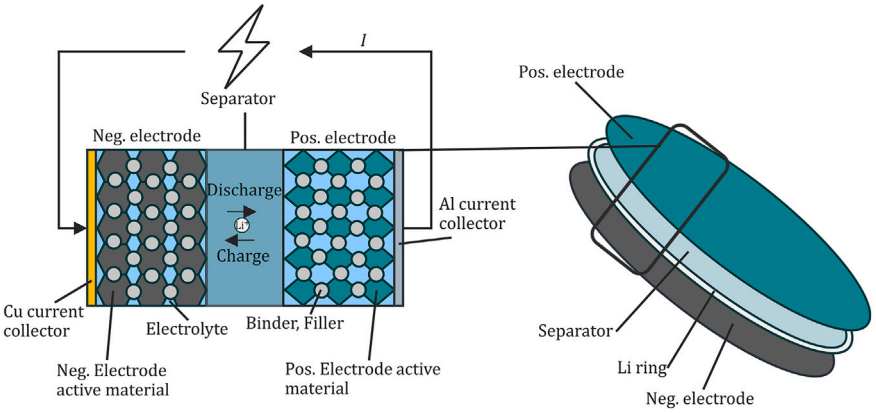

Fig. 1. Schematic of the three-electrode coin cell used in this article. The cell components (electrodes and separator) are 18mm disks, and a lithium ring attached to the separator serves as the reference electrode for measurements of the electrode potentials.

During graphite lithiation, the electrode material transitions through several distinct phases (denoted by Li_xC_6, for stoichiometries $x \in [0, 1]$), where each phase has different electrochemical properties [6]. The electrode material is not homogeneous, but consists of a large number of primary (sub-) particles. Due to nonlinear reaction kinetics, not all primary particles will in general be in the same phase, introducing phase separation in the material [7–9]. It is only in the final stage (LiC_6) that the graphite particles risk being plated, making it interesting to track the phase evolution during fast-charging [10].

The phase content of an electrode can be measured using techniques such as X-ray diffraction (XRD) [11–14], neutron diffraction [15,16], and nuclear magnetic resonance [17]. Although measurements of phase content are possible in operando, these devices cannot be included in any battery management system (BMS) because of cost and size limitations. Additionally, using high-energy X-rays to perform operando diffraction experiments may induce local beam effects in the material [18], which can affect the reliability and relevance of the results obtained with operando XRD.

Another commonly used method for the analysis of LIB phase transitions is incremental capacity analysis (ICA), which can also be used to monitor battery degradation [19,20]. Peaks in the IC curve can be attributed to phase changes in the electrode. However, the peaks become less identifiable as the cell ages or at higher currents [20]. This limits the utility of ICA for phase characterization to low currents and fresh cells. A further limitation of peak identification with ICA is that the method doesn't directly yield the amount of each phase present in the electrode.

In this work, we propose a novel method for estimating the phase evolution of graphite electrodes from electrochemical signals during constant-current (CC) charging, which can be readily measured during the charge process of LIBs. The method is based on phase characterization with ICA and utilizes how electrochemical signals become smoother at higher currents to estimate the phase evolution when ICA is not applicable, by fitting the parameters of a logit-normal kernel density function (KDF). The results show that we can accurately estimate the phase content above 35% state of charge (SOC) for charging rates up to C/5 (a 5 hour C-rate), for which the estimation is validated using a physics-based model [21]. Above C/5 , the model assumptions hinder validation, but applied to coin cell experiments we show that the fitted standard deviation of the KDF increases with current, which reflects the expected increase in inhomogeneity at higher currents.

2. Modeling and experiments

In this section, we briefly introduce the multiphase intercalation reaction of LIBs with graphite electrodes. We then describe the physics-based simulation model used in this study. Finally, the experiments performed to validate our estimation method are explained.

Table 1
Crystal structure properties of lithiated graphite: Li-graphite intercalation compound and stoichiometry of phase transition (x in Li_xC_6) [22], and unit cell volume [23]. The stages are grouped into four phases, shown in the leftmost column, based on similarities in their crystal structure.

Phase group	Material stage	LiC_p	x	Unit cell volume [Å^3]
Phase 4	Graphite	C_6	0	35.3
	Stage 1L	$LiC_{288–72}$	0.063	35.6
Phase 3	Stages 8L–5L	$LiC_{72–45}$	0.13	36.2
	Stage 4L	LiC_{36}	0.18	36.3
	Stage 3L	LiC_{27}	0.23	36.6
	Stage 2L	LiC_{18}	0.25	36.9
Phase 2	Stage 2	LiC_{12}	0.50	37.4
Phase 1	Stage 1	LiC_6	1	39.9

2.1. Lithium-ion batteries

The structure of the coin cell used in this study is shown in Fig. 1. When a LIB is charged, lithium is oxidized at the positive electrode and lithium ions are reduced (intercalated) at the negative electrode; the reverse reactions occur during discharge. For a LIB with graphite as the negative electrode and lithium nickel manganese cobalt oxide (NMC811) as the positive electrode, the charge (c) and discharge (d) reactions can be formulated as

$$Li_xC_6 \underset{c}{\overset{d}{\rightleftharpoons}} xLi^+ + xe^- + C_6, \tag{1}$$

$$Li_zNi_{0.8}Mn_{0.1}Co_{0.1}O_2 + (1-z)Li^+ + (1-z)e^- \underset{c}{\overset{d}{\rightleftharpoons}} LiNi_{0.8}Mn_{0.1}Co_{0.1}O_2. \tag{2}$$

Here, the stoichiometric states x and z indicate the charge level of each electrode, with $x = 1$ representing a fully charged negative electrode composed entirely of LiC_6.

During these reactions, both electrode materials transition between multiple stable phases as x and z change. In this study, we investigate the phase evolution of the negative electrode, whose phases are described in Table 1. Note that the molecular compound (LiC_p) is not necessarily constant for each phase, since x increases as the cell is lithiated. Instead, the phase designation refers to the crystal structure of the electrode. The different lithium-graphite intercalation compounds (Li-GICs) differ in staging structures; the stage number represents the number of graphene layers between each filled lithium layer and the "L" signifies that the lithium-ions are positioned in a disordered (liquid-like) structure. Based on their staging characteristics, the Li-GICs are categorized into four distinct phases: Graphite and Stage 1L are classified as Phase 4 and Stages 8L to 2L are grouped into Phase 3. Stage 2 is designated as Phase 2 and finally Stage 1 corresponds to Phase 1.

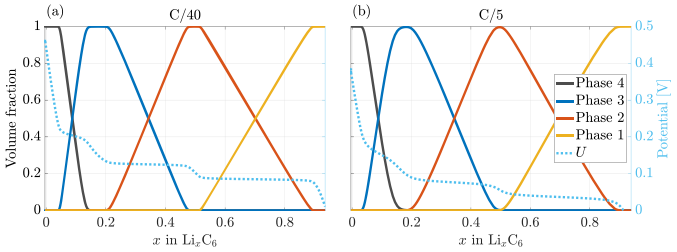

Fig. 2. Normalized volume fraction of phases and electrode potential (U) during **(a)** C/40 lithiation and **(b)** C/5 lithiation of a graphite half-cell, simulated using the model described in [21]. Four phases are considered: Phase 4 (graphite and Stage 1L), Phase 3 (Stages 8L to 2L), Phase 2 (Stage 2), and Phase 1 (Stage 1). The Li-GIC stages are described further in Table 1.

The distribution of electrode phases is inhomogeneous even during slow (close to equilibrium) charging, and can be described by the Fokker-Planck equation [9]. In addition to the crystal structures the material phases also differ in electrochemical potential, leading to potential plateaus for stoichiometric ranges where multiple phases coexist, and potential slopes when a single phase is active [7]. The phase inhomogeneity increases with higher currents since the electrode is no longer at equilibrium, which smooths the phase evolution and the potential profile. This effect is illustrated in Fig. 2, where the phase evolution and electrode potential during C/40 and C/5 lithiation of a graphite half-cell are shown. Similar smoothing effects have also been observed in operando diffraction studies at high C-rates [24]. The increased inhomogeneity is caused by nonlinearities in the intercalation reaction, which yield a higher degree of phase separation as the current increases [10].

Since smoothing of both the electrode phase evolution and potential is caused by the increased inhomogeneity at higher currents, we hypothesize that smoothing is similar for these properties. This leads to the formulation of our estimation method.

2.2. Physics-based model

To validate the estimation method, we simulate the phase evolution of a graphite half-cell using the reaction-limited model described in [21], for which the simulated C/20 phase evolution has been validated against operando XRD measurements. The model is based on the single-particle assumption and neglects electrolyte and temperature dynamics, which limits its applicability to low currents. The reaction limitation means that diffusion is assumed to be infinitely fast in the electrode, removing the spatial dependence of the (normalized) lithium concentration $\bar{c} \in [0, 1]$ in the primary particles. At higher currents, these assumptions may no longer hold, as diffusion limitations in the electrolyte produce a changing electrolyte concentration across the porous electrode depth and shrinking-core patterns may emerge inside the graphite particles due to mass-transport limitations in the solid electrode [7,10]. Furthermore, at high currents ohmic losses become significant, which may result in an increased battery temperature, violating the constant temperature assumption. These model limitations are, however, mitigated by limiting the current to low C-rates; in this study, we perform simulations for the currents C/40–C/5.

The model describes how the population density of the lithium concentration in the electrode evolves during its lithiation, that is, the probability distribution of $\bar{c}$ over time: $p(\bar{c}; t) = \rho(\bar{c}, t)$, where $\rho(\bar{c}, t)$ is governed by the Fokker-Planck equation [9]. This holds when the number of primary particles $n_p \to \infty$; note that this is different from the number of secondary particles (which is assumed to be one) [21]. For phase-separating materials, such as Li_xC_6, the population density is multimodal, with each mode corresponding to a phase of the material. Therefore, the volume fraction of each phase can be calculated by integrating the population density over the concentration range of each phase:

$$p_i(t) = \int_{lb_i}^{ub_i} \rho(\bar{c}, t) d\bar{c}, \tag{3}$$

where lb_i and ub_i are the lower and upper bounds of Phase i (as defined in Table 2), these are selected as the concentrations where $\rho(\bar{c}, t)$ is minimized between each phase peak. The volume fraction calculation is illustrated in Fig. 3, which shows the electrode potential, phase evolution, and population density during simulated C/40 lithiation.

Table 2
Integration bounds used when calculating the phase content from the population density.

Phase	4	3	2	1
Lower bound	0	0.15	0.37	0.65
Upper bound	0.15	0.37	0.65	1

2.3. Experimental setup

The electrode and electrolyte materials used in this study were carefully selected and processed to ensure consistent electrochemical performance. The electrode materials were punched into disks 18mm in diameter from sheets provided by CustomCells Itzehoe GmbH. The negative electrode (graphite) consisted of 95 wt.% active material, with a density of 1.7 g/cm^3, an areal capacity of 2.5 mAh/cm^2, and a copper current collector. The positive electrode (NMC811) was made of 96 wt.% active material, had a density of 2.9 g/cm^3, an areal capacity of 2.0 mAh/cm^2, and an aluminum current collector. Lithium hexafluorophosphate ($LiPF_6$) in a 50:50 wt.% mixture of ethylene carbonate and dimethyl carbonate (LP50) was used as electrolyte (E-Lyte Innovations GmbH).

The cell was assembled in a PAT-Cell-Force holder (El-Cell GmbH), an electrochemical cycler that supports three-electrode coin cell and enables measurements of cell expansion. Measurements and control of the PAT-Cell-Force were performed using a PAT-Channel-1 (El-Cell GmbH). The reference electrode consisted of a lithium ring attached to a 260 µm thick borosilicate glass fiber separator (Whatman FG/A), both held together by a polypropylene (PP) insulation sleeve (El-Cell GmbH). After assembly, the initial force applied by the PAT-Cell was set to 52.64 N and a formation cycle was performed following the recommended procedure provided by CustomCells. This initial cycle was run to allow a solid electrolyte interface (SEI) to form gradually on the electrodes, preventing more severe degradation during subsequent cycling. All assembly processes were performed in an argon-filled glovebox (Vigor Technologies Inc.) and the cell was cycled in a thermal chamber (LHU-124, ESPEC Corp.) maintained at 25 °C. A schematic of the three-electrode coin cell used in the experiments is shown in Fig. 1.

Following formation, seven constant-current constant-voltage (CC-CV) charge and discharge cycles were run at C-rates C/60, C/40, C/20, C/10, C/5, C/2, and 1C (5mA), using the same voltage limits as in the formation cycle (3V and 4.2V), with CV held until the current was below C/100. Between each charge and discharge, the battery was rested for 10 minutes to reduce any remaining concentration gradients.

2.4. Data processing

The electrode SOC was not directly measurable using the experimental setup, instead it was estimated using Coulomb-counting combined with an affine mapping to align the estimated SOC with known phase transitions of the electrode material:

$$x(t) = A\hat{x}(t) + B, \quad \hat{x}(t) \approx \frac{1}{C}\int_0^t I(\tau) d\tau, \tag{4}$$

where $\hat{x}(t)$ is the SOC estimation from Coulomb-counting, C is the nominal cell capacity, and $I(\tau)$ is the applied current at time τ. The affine

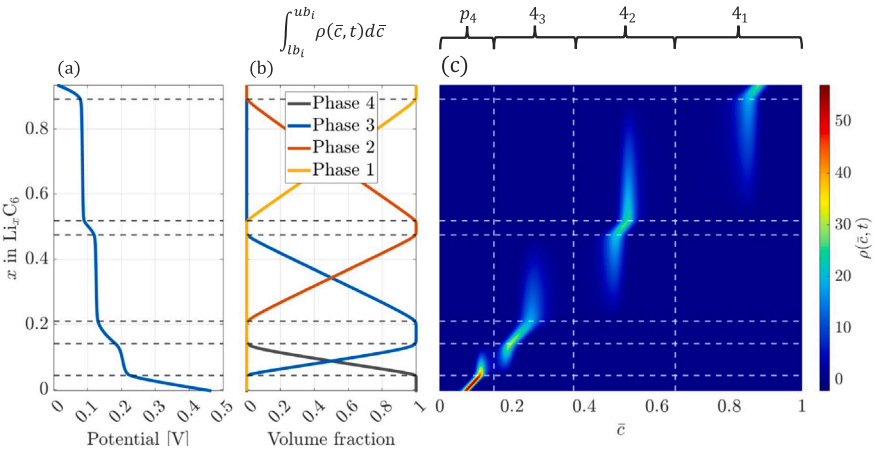

Fig. 3. (a) electrode potential, **(b)** calculated phase evolution, and **(c)** population density $\rho(\bar{c},t)$ during simulated C/40 lithiation of a graphite half-cell. The phase evolution is obtained by integrating the population density over the normalized concentration range for each phase, as defined in Table 2.

mapping $A\hat{x}(t)+B$ was evaluated using known SOC locations of phase transitions specified in [22], enabling phase identification:

$$A = 0.4167/(\hat{x}_{50}-\hat{x}_8), \quad B = 0.5 - A\hat{x}_{50}, \tag{5}$$

where $\hat{x}_{50}$ and $\hat{x}_8$ are the Coulomb-counting SOC locations for the dU/dx peaks associated with stoichiometries $x = 0.5$ and $x = 0.0833$, respectively. The A and B coefficients were determined using the reference measurement C/40 and the same transformation was applied to all measurements (C/40–1C). This step is not necessary for the simulated data, as the lithium filling fraction is then directly available to be used as SOC.

Further peak alignment was performed for C-rates above C/40 using dynamic time warping (DTW) to reduce drift introduced in the SOC reconstruction. This was implemented using the MATLAB `dtw` function [25] to find the best constant SOC-shift that aligns the first dU/dx peak of each higher current measurement with the first dU/dx peak of the C/40 measurement. Prior to the calculation of dU/dx, potential measurements (U) are smoothed using a Savitzky-Golay filter [26] to limit the amplification of measurement noise in the differentiation process. This signal smoothing is only applied for visual purposes, to reduce the distortion of noise in the dU/dx profiles, as the usage of a high forgetting factor in the phase estimation (see Section 3.2) limits the impact of noise on the estimation results. An illustration of the reference and target SOC-adjustments can be found in Appendix A, Fig. A.1.

The peak locations $\hat{x}_{50} \approx 0.547$ and $\hat{x}_8 \approx 0.0933$ were found using the MATLAB `findpeaks` function [27], resulting in $A \approx 0.919$ and $B \approx -0.00240$ by insertion into Eq. (5). A similar transformation was also applied to the simulated SOC-sequence to enable comparison between simulated and experimental data. This was performed so that the peak locations of the C/40 simulation match the C/40 measurement. The parameters $A^{\text{sim}} \approx 1.16$ and $B^{\text{sim}} \approx -0.085$ were used for this transformation, these were calculated from the SOC-locations $x_{50}^{\text{sim}} \approx 0.505$ and $x_8^{\text{sim}} \approx 0.145$. Such scaling needs to be applied since the assembled cell used in our experiments and the cell used to tune the simulation model have slightly different electrical properties due to manufacturing-induced variations. Also note the discrepancy between x_8^{sim} and $x = 0.0833$; this may be caused by model simplifications of the phase evolution at low SOC (see [21]). These simplifications influence the simulated dU/dx as peaks in dx/dU correspond to phase transitions in the material. The simulation SOC-adjustments are demonstrated in Appendix A, Fig. A.3.

3. Estimation method

The objective is to estimate the phase evolution of a graphite electrode during its lithiation. The method utilizes the smoothing effect described previously in Section 2.1, where both the electrode phase distribution and potential become smoother at higher currents due to increased inhomogeneity. The estimation is performed in three steps:

1. Two charging cycles are performed: one at low current (the reference), so that ICA can be utilized for phase characterization; and one at any higher current (the target). The target measurement may be performed online, but the reference measurement that is used in the estimation of the target phase evolution must be performed offline.
2. ICA is performed on the reference measurement to identify the knee-points of the peaks in the IC curve. These locations are used to construct a piecewise linear approximation of the reference phase evolution.
3. A logit-normal KDF is fitted so that the smoothed reference signal using the KDF matches the target signal in a least squares sense. The logit-normal KDF is used as it bounds the random variable between 0 and 1 where the endpoints cannot be obtained. This matches the thermodynamic description of the electrode filling fraction $x \in [0,1]$ as the chemical potential of the intercalation reaction diverges when $x \to 0$ and $x \to 1$ [7]. Once fitted, the KDF is used to smooth the estimated reference phase evolution, resulting in an estimation of the target phase content.

These steps are illustrated in Fig. 4. Note that the estimation method assumes CC charging is applied during constant temperature conditions. If the current profile changes with time, the voltage profile will change instantaneously due to ohmic losses in the cell. These need to be compensated for before applying the phase estimation method since any voltage offset will influence the fitting parameter of the smoothing kernel. Similar compensation should also be applied if the cell temperature changes drastically, which will likely be the case when higher charging currents (>1C) are applied.

The choice of density kernel is important for the phase estimation performance. For example, if a truncated Gaussian is used, skewness will not be introduced close to the SOC edges since the Gaussian kernel is fundamentally a symmetric distribution, see Appendix B, Fig. B.1. Compared to the logit-normal kernel, the Gaussian kernel always varies equally around the mean μ, independently of where μ is positioned on the interval $x \in [0,1]$. This forced symmetry can yield too high probability weight to measurements close to the SOC edges, where it is instead expected that the distribution should have a tail towards the center of the interval. This issue can be resolved by, for example, using the logit-normal distribution as the kernel instead [28]. Another bounded KDF candidate which incorporates skewness is the beta distribution [29],

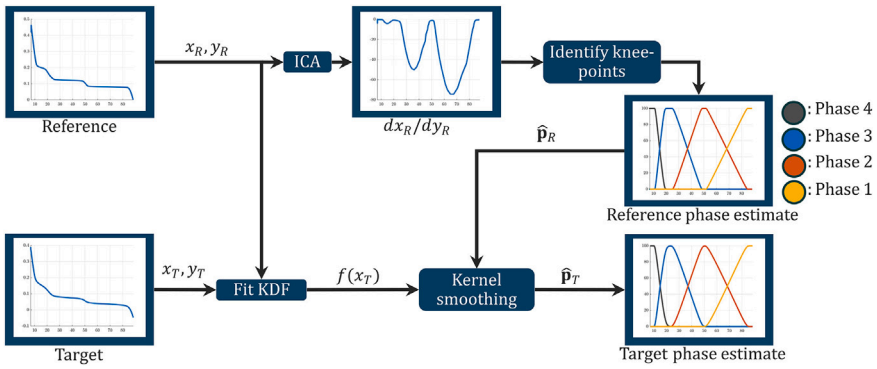

Fig. 4. Diagram of the proposed estimation method. Phase identification for the target measurement is performed by smoothing the reference measurement. The vectors $\hat{\mathbf{p}}_R$ and $\hat{\mathbf{p}}_T$ contain the estimated phase content of the reference and target measurements, respectively, for Phases 1 to 4.

which is compared to the logit-normal kernel and the truncated Gaussian kernel in the same figure. Since the determination of the beta distribution requires the computation of $\text{Beta}(\alpha,\beta) = \Gamma(\alpha)\Gamma(\beta)/\Gamma(\alpha+\beta)$, fitting the beta distribution parameters becomes numerically problematic if either α or β grows large, which motivates the choice of the logit-normal distribution instead. Note that other kernel choices are possible, for example the skewness could be set as a distribution parameter, but we limit the investigation to two-parameter distributions to simplify the fitting problem.

3.1. Estimating the reference phases

To enable the use of ICA for phase characterization, the reference measurement must be performed at a low C-rate [20], as above C/6 the peaks become less identifiable due to increasing phase inhomogeneity. Ideally, even lower rates (e.g., below C/20) should be used, so that the electrode potential approximates its open circuit potential, i.e., the cell is at a quasi-steady state.

Given electrode potential (U_k) and charge (Q_k) measurements at times t_k, the IC curve (dQ/dU) is calculated as $dQ/dU(t_k) = (dQ/dt)/(dU/dt)(t_k) \approx I(t_{k-1})(t_k - t_{k-1})/(U_k - U_{k-1})$, where $I(t_{k-1})$ is the applied current.

Both simulation [10,11,30] and experimental [12,13,15,16,23] studies indicate that, at low C-rates, the graphite electrode exhibits at most two coexisting phases. This staging behavior follows from the thermodynamics of multiphase systems, where two-phase coexistence arises between the minima of the Gibbs free energy profile [7,21]. Within the two-phase regions, the phase content changes linearly with respect to the stoichiometry x, as mass conservation forces a decrease of e.g., Phase 4 content to result in a corresponding increase of Phase 3 content, since the phases are directly related to the stoichiometry through their molecular composition (see Table 1). These conditions hold exactly at equilibrium, and approximately close to equilibrium, as is seen for the C/40 simulation in Fig. 5. Assuming that both conditions hold, it is sufficient to find the knee-points of the phase peaks in Fig. 5 to determine a piecewise linear approximation of the phase evolution at low C-rates.

By inspection, the knee-points of the IC curve in Fig. 5(a) correspond well in SOC to the knee-points of the phase transitions. Thus, the IC knee-points may be used to estimate the phase evolution of the reference. To locate the knee-points, the Bacon and Watts model [31] is fitted to each interval between the extreme points of the IC curve, which are found using MATLAB's `findpeaks` function [27]. That is, the following optimization problem is solved:

$$\min_{\alpha_0,\alpha_1,\alpha_2,x_0} \sum_{k=1}^{n} \left[y_k - \alpha_0 - \alpha_1(x_k - x_0) - \alpha_2 \tanh\left(\frac{x_k - x_0}{\gamma}\right)\right]^2, \tag{6}$$

for SOC and IC measurements $\{x_k, y_k\}_{k=1}^n$ between the extreme points of the IC curve. The parameter γ is chosen to be small so that

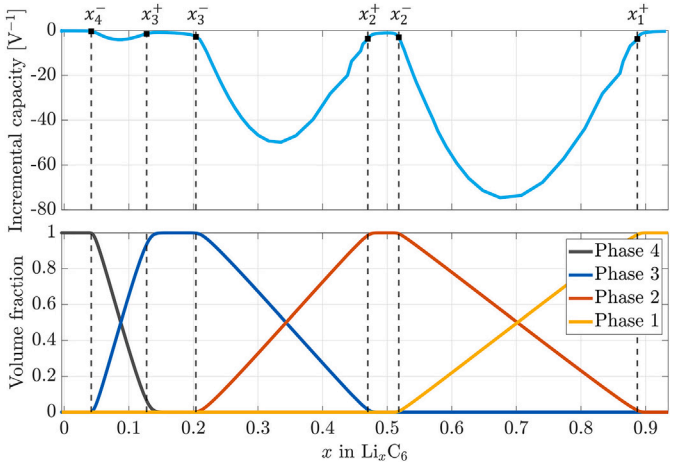

Fig. 5. Normalized volume fraction of phases during C/40 lithiation of a graphite half-cell, plotted together with the IC profile (dx/dU). Peaks in the IC curve align with phase transitions, and the knee-point locations (marked with dotted lines) correspond well to the SOC locations of the knee-points of the phase evolution.

$\tanh((x_k - x_0)/\gamma)$ smoothly approximates $\text{sgn}(x_k - x_0)$. The optimization variables are $\alpha_0, \alpha_1, \alpha_2$, and x_0, where x_0 is the knee-point location.

Given left and right knee-points x_i^+ and x_i^- of Phase i (illustrated in Fig. 5), the piecewise linear approximation of its volume fraction $\hat{p}_i(x)$ is defined as

$$\hat{p}_i(x) = \begin{cases} \frac{x - x_{i+1}^-}{x_i^+ - x_{i+1}^-}, & x_{i+1}^- \le x < x_i^+, \\ 1, & x_i^+ \le x < x_i^-, \\ \frac{x_{i-1}^+ - x}{x_{i-1}^+ - x_i^-}, & x_i^- \le x < x_{i-1}^+, \\ 0, & \text{otherwise.} \end{cases} \tag{7}$$

Note that there is no left knee-point for Phase 4, so $\hat{p}_4(x) = 1$ for $0 \le x < x_4^-$. Similarly, Phase 1 has no right knee-point, so $\hat{p}_1(x) = 1$ for $x_1^+ \le x \le 1$.

3.2. Fitting the smoothing kernel

Let $x_R(t)$ and $y_R(t)$ define the reference SOC and electrochemical signal (e.g., as in Fig. 2(a)), and let $x_T(t)$ and $y_T(t)$ represent the corresponding measurements for the target (e.g., as in Fig. 2(b)).

Given the piecewise linear approximation of the reference phase evolution $\hat{p}_i^R(t)$, the goal is to estimate the target phase evolution by smoothing the reference phase evolution using a logit-normal distribution as

KDF [28], defined as

$$f_{\mu,\sigma}(x_R) = \frac{1}{x_R(1-x_R)\sqrt{2\pi\sigma^2}} \exp\left(-\frac{(\text{logit}(x_R)-\mu)^2}{2\sigma^2}\right)\frac{1}{Z(\mu,\sigma)}, \tag{8}$$

where σ is the smoothing parameter to be fitted, $Z(\mu,\sigma)$ is a normalization constant, and $\mu = \text{logit}(x_T)$ is the inverse logistic transformation of the target SOC: $\text{logit}(x_T) = \log\left(x_T/(1-x_T)\right)$ for $x_T \in (0,1)$, which is always satisfied since x_T represents the electrode SOC. The normalization constant $Z(\mu,\sigma)$ is introduced because the set of reference measurements $\mathbb{X}_R = \{x_R(t)\}$ may be smaller than the interval (0,1). It is calculated from the logit-normal cumulative density function (CDF)

$$Z(\mu,\sigma) = \frac{1}{2}\left[\text{erf}\left(\frac{\text{logit}(\max(\mathbb{X}_R))-\mu}{\sqrt{2\sigma^2}}\right) - \text{erf}\left(\frac{\text{logit}(\min(\mathbb{X}_R))-\mu}{\sqrt{2\sigma^2}}\right)\right], \tag{9}$$

where erf(·) is the error function. This ensures that $f_{\mu,\sigma}$ satisfies $\int_{\mathbb{X}_R} f_{\mu,\sigma}(x)dx = 1$.

The distribution $f_{\mu,\sigma}$ models the logit of x_R as normally distributed, thus ensuring $x_R \in (0,1)$. This matches the physical description of the electrode SOC because neither the fully discharged nor fully charged states can occur during normal battery usage. The KDF is used to smooth the reference signal so that the expected value of y_R over $f_{\mu,\sigma}$ matches the target signal y_T, minimizing the squared estimation error, i.e.

$$e_y^2(t;\mu,\sigma) = (\mathbb{E}_{f_{\mu,\sigma}}[y_R] - y_T(t))^2, \text{ where } \mathbb{E}_{f_{\mu,\sigma}}[y_R] = \int_{\mathbb{X}_R} y_R(x) f_{\mu,\sigma}(x)dx. \tag{10}$$

To penalize rapid changes in σ, a forgetting factor $\lambda_k \in [0,1]$ is introduced. The kernel fitting problem is then formulated as

$$\min_{\sigma_t>0} \sum_{k=0}^{n-1} \lambda_k^{|t-k|} e_y^2(k;\text{logit}(x_T(k)),\sigma_t), \tag{P}$$

which is solved for each target measurement x_T and y_T, where t is the time index, and n is the length of the target measurement set. Note that λ_k can be varied, as indicated by the subscript k. For online estimation $n = t$.

The optimization problem (P) is nonlinear and nonconvex in general; it is solved using MATLAB's unconstrained `fminsearch` routine [32]. The possible nonconvexity implies that the solver is only guaranteed to converge to a local minimum, which makes the solution sensitive to the initial guess. This may in turn introduce discontinuities in σ_t^* over time. To alleviate this problem, the forgetting factor λ_k may be set high, which reduces the nonconvexity of the problem since large changes in σ_t will be penalized. This "convexification" effect is illustrated in Appendix A, Fig. A.4. Besides the benefit of improved convexity, a large forgetting factor also makes the optimization problem less sensitive to noise, which is illustrated in Appendix A, Figs. A.5 and A.6.

The solution in the previous time-step, σ_{t-1}^*, is used as initial guess for σ_t^*. This choice is made since σ_t quantifies how y_T is smoothed compared to y_R; thus, σ_t^* should vary smoothly unless $y_T(t)$ contains discontinuities (e.g., if the current changes). When $t = 0$, no previous measurement exists; instead, $\sigma_0 = 0.01$ is provided as initial guess to the solver. To satisfy the constraint $\sigma_t > 0$, we simply apply the absolute value to the solver output since σ_t only appears squared in $e_y^2(k;\text{logit}(x_T(k)),\sigma_t)$. Once the optimum σ_t^* is found, the target phase content is estimated by smoothing the estimated reference phase evolution:

$$\hat{p}_i^T(t) = \mathbb{E}_{f_{\mu_t,\sigma_t^*}}[\hat{p}_i^R], \text{ for } i = 1,\dots,4. \tag{11}$$

This means that we model the smoothing effect of y_T as purely caused by the distribution of the material phases, p_i^T. Given that y_T is the electrode potential and conductivity is high, this assumption holds, as the electrode potential is determined by the chemical potential of the ensemble of the primary particles, which is directly related to the phase distribution in the material: $\rho(\bar{c},t)$ [9,21]. Since f_{μ_t,σ_t^*} is used to smooth the reference phase evolution $\hat{p}_i^R$, the variance of f_{μ_t,σ_t^*} may then be interpreted as how the width of the lithium concentration distribution $\rho(\bar{c},t)$ is changed for the target measurement, compared to the reference measurement. That is, it may serve as a proxy for increased lithiation inhomogeneity in the target measurement. The sought variance is, however, different from $(\sigma_t^*)^2$ since σ_t^* describes the standard deviation of $\text{logit}(x_R)$.

3.2.1. Variance estimation

The standard deviation σ_t found by solving (P) is the standard deviation of $\text{logit}(x_R)$. We are, however, interested in the standard deviation of x_R since this can indicate inhomogeneity in the electrode lithiation, but no analytical expression exists for the logit-normal distribution. Instead, the m-th moment of the distribution may be approximated by a quasi-Monte Carlo estimate [33]: $\mathbb{E}_{f_{\mu,\sigma}}\left[x_R^m\right] \approx \frac{1}{K-1}\sum_{k=1}^{K-1}\left(\text{L}\left(\Phi_{\mu,\sigma}^{-1}(k/K)\right)\right)^m$, where K is the number of approximation points (chosen as the length of the reference measurement vector), $\text{L}(x) = \exp(x)/(1+\exp(x))$ is the standard logistic function, and $\Phi_{\mu,\sigma}^{-1}$ is the inverse CDF of the normal distribution with mean μ and standard deviation σ.

After estimating the first and second moments of x_R, the standard deviation σ_R is found as $\sigma_R = \sqrt{\text{Var}(x_r)}$, where $\text{Var}(x_r) = \mathbb{E}_{f_{\mu,\sigma}}[x_R^2] - \mathbb{E}_{f_{\mu,\sigma}}[x_R]^2$.

4. Results and discussion

We validate our method for graphite electrodes using physics-based half-cell simulations and experimental data from a three-electrode coin cell, where the negative electrode potential is approximated as the potential difference between the reference electrode and the negative current collector (see Fig. 1). Our findings show that the estimation results for low current experimental data (below C/2) agree well with the theoretical results for mid to high range SOC. Definitions of the evaluation metrics used in the results section are found in Appendix C.

4.1. Half-cell simulations

We simulate half-cell lithiation for C-rates ranging from C/40 to C/5, using the reaction-limited model described in [21]. The C/40 profiles serve as the reference for estimating the phase evolution at higher C-rates (C/20, C/10, and C/5). The fitting is performed for both the electrode potential and its derivative (dU/dx). To account for the current-dependent potential drop due to ohmic losses, the target potential profiles are linearly adjusted so that y_T at the end of charge matches y_R.

The reference and target data are sampled equidistantly with step size $\Delta x \approx 0.003$ (in total 250 samples). A variable forgetting factor $\lambda_k = \min(0.99, 0.2\cdot 1.1^{100x_T(k)}, 0.2\cdot 1.1^{100(1-x_T(k))})$ is used to penalize rapid changes in σ_t. The symmetric exponential change in λ_k allows faster changes in σ_t at the beginning and the end of charge where the electrode inhomogeneity is expected to be lower due to the proximity to the SOC bounds (0,1), and the maximum value of $\lambda_k = 0.99$ ensures that the optimization problem remains convex, which means that `fminsearch` finds the optimal σ_t.

4.1.1. Reference phase estimation

The IC curve, the ground truth phase evolution, and the piecewise linear estimation of the phase evolution are presented for the reference simulation in Fig. 6. The estimated phase evolution closely matches the ground truth, achieving a mean absolute error of $\text{MAE}(\hat{p}^R) \approx 1.92$ percentage points (%pt.), which implies a MAE of 0.96%pt. per phase since two phases are active at a time. The largest estimation errors occur in the phase mixture regions and can be attributed to two main factors:

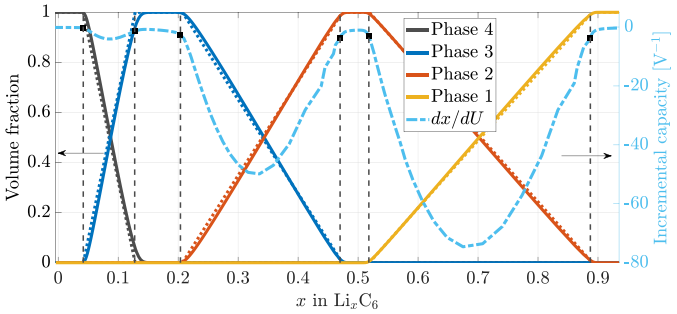

Fig. 6. Normalized volume fraction of phases (solid lines) for the reference simulation (C/40), plotted alongside IC (dx/dU) and estimated volume fractions (dotted lines). Black squares indicate the knee-points of the IC curve, which were used to compute the estimated phase fractions via Eq. (7). (For interpretation of the references to color in this figure legend, the reader is referred to the web version of this article.)

Table 3
Absolute difference between true and estimated knee-point locations (in SOC), where true knee-points are defined as the first SOC where $p_i^R > 0.997$.

Knee-point	x_4^-	x_3^+	x_3^-	x_2^+	x_2^-	x_1^+
True	0.0425	0.144	0.205	0.477	0.515	0.892
Estimated	0.0419	0.128	0.204	0.470	0.518	0.887
Error	0.000669	0.0164	0.00133	0.00675	0.00318	0.00448

first, the ground truth phase evolution is smooth, whereas the estimated phase evolution is piecewise linear, and thus non-differentiable at each knee-point; second, the knee-point locations identified via ICA do not perfectly align with the true phase knee-points. Among these, the first factor is likely dominant, as the knee-point location errors are small (see Table 3).

4.1.2. Target phase estimation

Plots of the measured and fitted C/5 potential and differential potential are shown in Fig. 7 (see Appendix D, Figs. D.1 and D.2 for lower C-rates). A close fit is found for both signals, though, the phase estimation performance is consistently worse for the electrode potential

Table 4
Mean of fitted σ_R, MAE of curve fit (y_T), and phase prediction ($\hat{p}^T$), for different C-rates, and for different signals (Potential: U; differential potential: dU/dx).

	Mean(σ_R)		MAE(y_T)		MAE($\hat{p}^T$)	
C-rate	U	dU/dx	U	dU/dx	U	dU/dx
C/20	0.00269	0.00214	0.00306	0.0313	1.92	1.92
C/10	0.0188	0.00790	0.0131	0.0775	2.40	2.34
C/5	0.0288	0.0229	0.0366	0.140	3.73	3.37

(particularly around $x = 0.5$). For both signals, the fitting and estimation performance are summarized in Table 4, and the phase estimation errors are plotted together with the estimated standard deviation σ_R in Fig. 8.

The results in Table 4 show that the standard deviation σ_R increases with the charging current, reflecting the expected increase in phase inhomogeneity. It is also observed that the standard deviation is of similar magnitude for the potential and differential potential, indicating that the average smoothing is comparable for these properties. Both MAE(y_T) and MAE($\hat{p}^T$) increase with current, although the phase estimation error is larger for the potential signal. Fig. 8 shows that the phase estimation performance is similar at low SOC, where σ_R is close between both signals, but for $x > 0.15$ the estimation error is higher using the potential signal, particularly around $x = 0.5$. The increase may be partly caused by the ohmic offset compensation used for the potential signal and, thus, the estimation error could likely be reduced by improving the adjustment. However, the offset problem is avoided by using the differential potential due to differentiation, and thus only the dU/dx signal will be used for phase estimation of the experimental data. In Fig. 8 it can also be seen that σ_R decreases at low and high SOC, suggesting that the inhomogeneity is lower close to the SOC limits.

4.2. Coin cell experiments

Next, we apply our phase estimation method to experimental data obtained from the three-electrode coin cell, where the negative electrode potential (U_n) is measured as the potential difference between the reference electrode and the negative terminal.

As with the simulated data, C/40 is used as the reference measurement. In addition to the previous target C-rates, C/2 and 1C are also

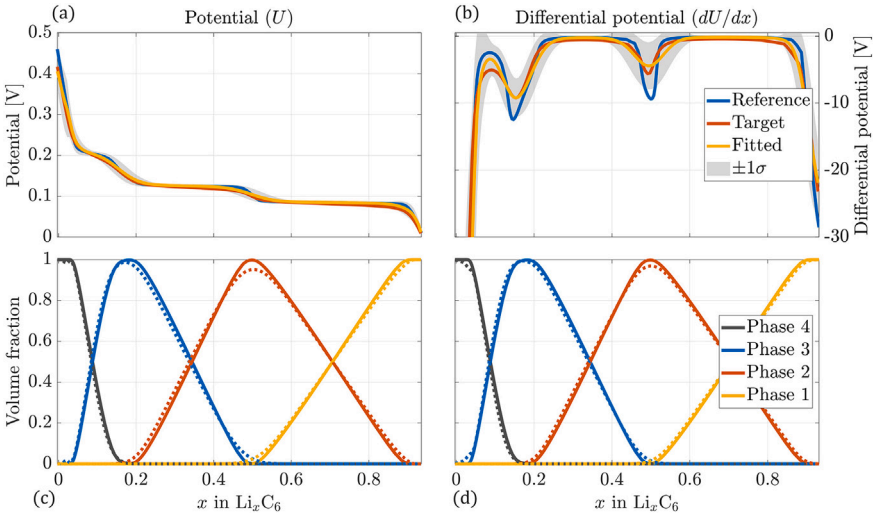

Fig. 7. Fitting and phase estimation results for simulated C/5 lithiation of a graphite half-cell, using electrode potential **(a,c)** and differential potential **(b,d)** to fit the KDF. C/40 was used as reference in both cases. In panels **(c)** and **(d)**, solid lines show the ground truth phase evolution, while dotted lines represent the estimated phase evolution.

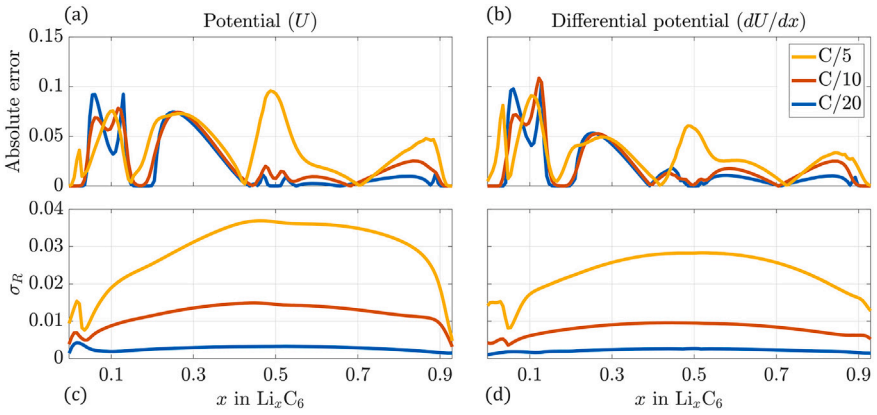

Fig. 8. Absolute phase estimation errors for simulated lithiation at rates C/20, C/10, and C/5 using C/40 as reference. Errors are shown for **(a)** electrode potential and **(b)** differential potential signals. Subfigures **(c)** and **(d)** display the corresponding standard deviations (σ_R) for each signal; the mean of σ_R is displayed in Table 4.

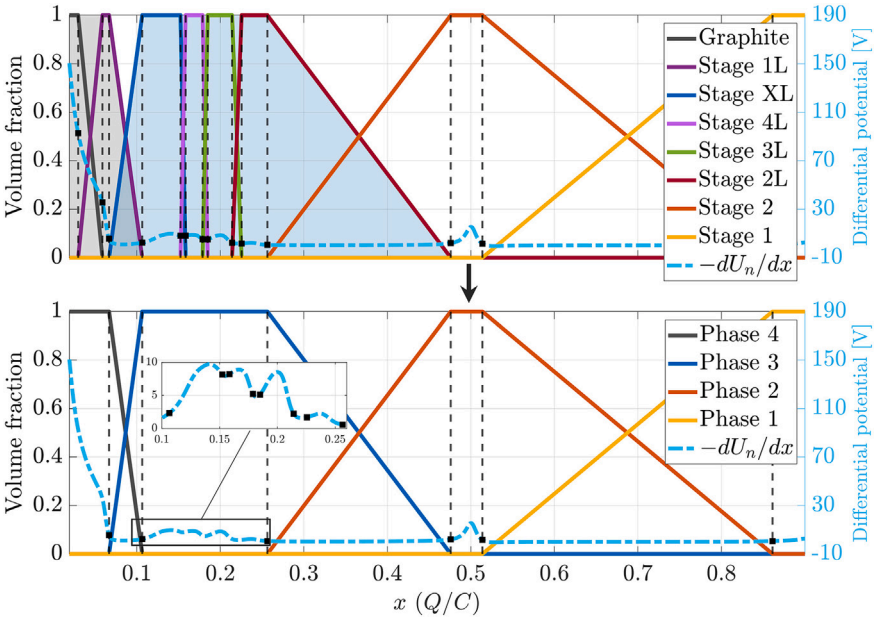

Fig. 9. Estimated volume fraction of phases for the reference measurement (C/40), plotted together with negative differential potential ($-dU_n/dx$). Black squares mark the knee-points used to compute phase fractions via Eq. (7). The upper plot includes additional stages (1L to 2L), which are grouped into Phases 4 and 3 in the lower plot, yielding a closer resemblance to the simulated phase evolution in Fig. 6. Some stages (e.g., 8L–5L) are not separable even at C/40 and are combined into a single peak ("Stage XL") in the upper plot. The inset in the lower plot shows a zoomed-in portion of the $-dU_n/dx$ profile for $0.1 \leq x \leq 0.26$, where several additional peaks are found compared to the simulated dx/dU in Fig. 6. (For interpretation of the references to color in this figure legend, the reader is referred to the web version of this article.)

included. Specifically, fitting of the experimental data is performed using dU_n/dx measurements. This avoids the need to correct for ohmic losses, which grow linearly with current and depend on the internal resistance of the cell, which in turn depends on SOC. The phase estimation is performed for a single measurement series.

As in the simulation case, a variable forgetting factor $\lambda_k = \min(0.99, 0.2 \cdot 1.1^{100x_T(k)}, 0.2 \cdot 1.1^{100(1-x_T(k))})$ is used to fit the KDF. The same discretization step size ($\Delta x = 0.003$.) is used for the reference and target data to ensure that the cost contribution from the forgetting factor is similar for the experimental and simulated cases, enabling comparison between the two.

4.2.1. Reference phase estimation

Measurements of $-dU_n/dx$ and the piecewise linear estimation of the reference phase evolution are shown in Fig. 9. Note that the knee-points of the $-dU_n/dx$ profile have been used instead of the IC profile. This choice was made due to the presence of a small region with $dU_n/dx > 0$ (approximately for $x \in [0.518, 541]$) in the reference measurement, which introduced discontinuities in the IC. Since IC= $1/(dU_n/dx)$, the knee-points of peaks in the IC curve correspond to knee-points of valleys in the dU_n/dx curve; this allows the peaks of $-dU_n/dx$ to be used for reference phase identification.

In the $-dU_n/dx$ profile of the reference measurement (Fig. 9), several additional peaks are observed compared to the simulated C/40 lithiation (Fig. 6). This discrepancy arises from limitations in the simulation model, where only one stable phase has been modeled in the range $x \in [0.1, 0.2]$. To enable a meaningful comparison between phase estimation using simulated and experimental data, the same grouping used in the simulation model (Phases 1–4) is applied to the experimental data through the following computations:

$$\hat{p}_4^R(x) = \hat{p}_{\text{Graphite}}^R(x) + \hat{p}_{1\text{L}}^R(x), \tag{12}$$

$$\hat{p}_3^R(x) = \hat{p}_{\mathrm{XL}}^R(x) + \hat{p}_{4\mathrm{L}}^R(x) + \hat{p}_{3\mathrm{L}}^R(x) + \hat{p}_{2\mathrm{L}}^R(x). \quad (13)$$

This results in the lower plot of Fig. 9, which more closely resembles the simulated phase evolution in Fig. 6. Due to the lower stability of the low stoichiometric stages (Stages 2L–XL), the assumption that only two phases are active at a time may not hold even at low C-rates [22]. However, by combining these stages into a single phase, the estimation errors of individual stages cancel: restoring the two-phase behavior. This can be seen in Fig. 9, where the peaks of Phase 4 and Phase 3 are separated by a distinct minimum in $-dU_n/dx$, representing a voltage plateau around $x = 1/12$; thus, the electrode exhibits a two-phase coexistence between the two merged phases.

4.2.2. Target phase estimation

The MAE of the curve fit and the mean of the standard deviation σ_R are presented for each target measurement in Table 5, and the fitting and phase estimation results for C/5, C/2, and 1C are shown in Fig. 10 (results for lower C-rates are shown in Appendix D, Fig. D.3). The estimated phase evolution and fitted σ_R are shown for all currents in Fig. 11.

As observed in the simulation results in Table 5, the standard deviation increases with charging current, most notably above C/5. Similarly, the fitting error also increases at higher currents. The lower plot of Fig. 11 reveals a significant increase in σ_R for C/2 and 1C, especially above $x > 0.25$ where a three-phase coexistence is predicted. Note again that Phase 3 includes Stages XL–2L, for which 3-stage coexistence is predicted starting from C/10 (see Appendix D, Fig. D.4 for the estimated evolution of all stages), due to the close proximity of the phase peaks. It is also observed that σ_R is lower close to the beginning and end of charge, which agrees with the fact that the electrode should be more homogeneous at low and high SOC.

Note that in addition to increased inhomogeneity, the increase of σ_R may also be caused by residual SOC misalignment after pre-processing, signal noise, or model mismatch, since σ_R is an inferred parameter from the measurement data. Due to the high forgetting factor (maximum $\lambda_k = 0.99$), the influence of noise is likely small. SOC misalignment and model mismatch may, however, play a larger part. In Appendix A, Fig. A.2, it is shown that the phase estimation is affected by SOC offsets between the reference and target measurement, in particular for low SOC where the magnitude of dU_n/dx is large. The mismatch at low SOC is small for all tested currents, since the CV cutoff is set to C/100 to ensure that each measurement starts from approximately the same SOC, and the DTW shift is performed to align the measurements for low SOC. At higher currents, in particular for C/2 and 1C, electrolyte dynamics start to influence the voltage profile, which may explain why the $|dU_n/dx|$ peak associated with the Phase 2–1 transition (around $x = 0.5$) shifts towards a lower SOC (see Fig. 10(b, c)). The peak is moved earlier since diffusion limitations in the electrolyte cause the electrode layers closest to the separator to lithiate earlier, while the electrode layers closer to the current collector lag behind. Thus, the single-particle simulation model we used for validation becomes a poor representation of the battery dynamics, and the estimation method may have to be adjusted to account for this polarization effect in the electrode material. In summary, this means that aside from an increase of σ_R due to increased lithiation inhomogeneity inside the secondary particles, electrolyte diffusion effects likely also influence the size of σ_R at higher currents since these cause lithiation heterogeneity across the secondary particles of the electrode. Another possibility at high currents is that shrinking-core effects may emerge in the electrode material, which also violate the reaction-limitation that was used in the physics-based model, and would further increase the lithiation heterogeneity among the electrode particles.

The fitted value of σ_R is also affected by temperature variations, cell aging, and variable currents. These factors are deemed to be small for our experiments since CC conditions are applied and the noise for current measurements with the PAT-Channel is negligible ($\Delta i < 100$ nA [34]), temperature variations are small (the total temperature variation is less than 0.25 °C across the seven cycles), and the estimation is performed on fresh cells. Before the method can be applied to realistic operating conditions, the contributions from these factors need to be compensated for (e.g., by adjusting the potential for temperature-dependent internal resistance losses and polarization).

Table 5
Mean of fitted σ_R and MAE of curve fit (y_T), for different C-rates. For the C/20 and C/5 measurements, the Fitting error of the first sample is significantly higher than all subsequent samples, and since the magnitude of y_k grows substantially for low SOC, these samples are discarded to avoid biasing the Fitting MAE towards this region. For more details, see Appendix D, Fig. D.5.

C-rate	C/20	C/10	C/5	C/2	1C
Mean(σ_R)	0.00350	0.00694	0.0127	0.0369	0.0633
MAE(y_T)	0.0469	0.0604	0.0616	0.130	0.158

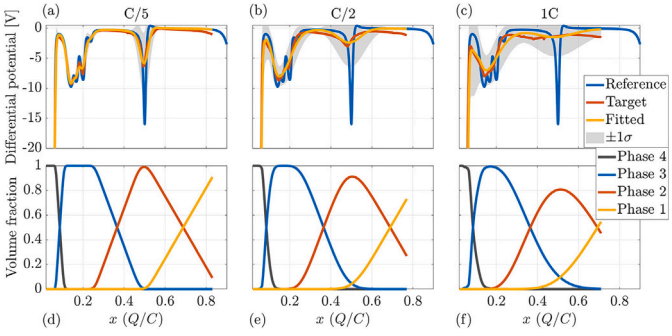

Fig. 10. Fitting and phase estimation results using differential negative electrode potential (dU_n/dx) measurements during C/5 **(a,d)**, C/2 **(b,e)**, and 1C **(c,f)**, using C/40 as reference.

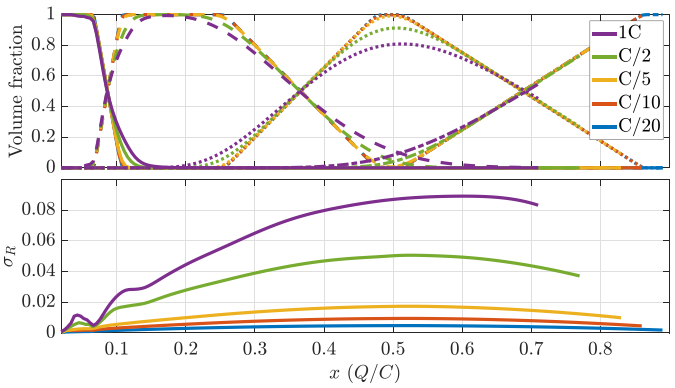

Fig. 11. Estimated phase evolution using differential voltage measurements at rates C/20, C/10, C/5, C/2, and 1C, using C/40 as reference. In the upper plot the different phases are differentiated by line styles: solid lines represent Phase 1, dashed lines represent Phase 2, dotted lines represent Phase 3, and dash-dotted lines represent Phase 4. The lower plot shows the corresponding standard deviations (σ_R); the mean of σ_R is found in Table 5.

4.3. Comparison with simulation

Comparing Tables 4 and 5, we found that the mean σ_R increases for both experiments and simulations, although σ_R is higher in the simulation results. This difference likely results from the dependence on SOC of σ_R. In simulations (Fig. 8(d)), σ_R remains relatively constant throughout the charging process, while the experimental results (Fig. 11) show that σ_R increases by an order of magnitude over the charging period: indicating that the electrode starts in a highly homogeneous state. The increased inhomogeneity can also be inferred directly from the dU_n/dx

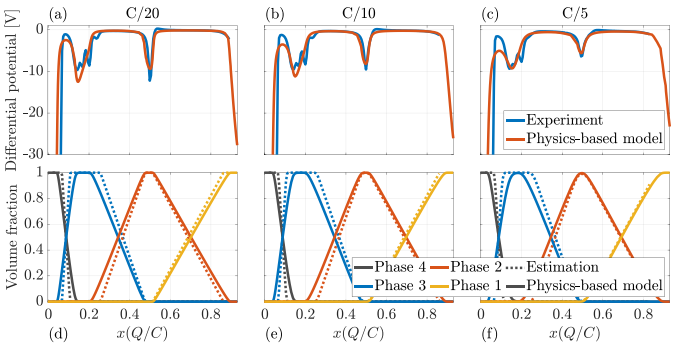

Fig. 12. Comparison of simulated differential half-cell potential (red) and experimentally measured differential negative electrode potential (blue) for C-rates **(a)** C/20, **(b)** C/10, and **(c)** C/5, and simulated phase evolution of a graphite half-cell (solid lines) and estimated phase evolution from coin cell measurements (dotted lines) at C-rates **(d)** C/20, **(e)** C/10, and **(f)** C/5. (For interpretation of the references to color in this figure legend, the reader is referred to the web version of this article.)

profiles in Fig. 10(a–c), as the reference and target dU_n/dx converge at low SOC ($x < 0.1$), but diverge at higher SOC. This contrasts with the simulation in Fig. 7(a, b), where the smoothing is present throughout the full SOC range, resulting in a higher current dependency of dU/dx in the initial charging period. In Appendix D, Fig. D.6, the differential potential profiles are compared for $x < 0.1$, which emphasizes the differences in the initial charging portion. The observed homogeneity at low SOC is consistent with the experimental conditions: due to the low CV discharge cutoff current (C/100), each charging cycle will begin from approximately the same low-SOC state. A similar increase in homogeneity is also perceived near full charge in both simulation and experimental results (see Figs. 8(c, d) and 11), this is also expected since Phase 1 represents a fully lithiated negative electrode.

Further comparison of simulated and experimentally measured dU_n/dx profiles is found in Fig. 12(a–c). For all currents, the largest difference is found at low SOC ($x \leq 0.25$), where several phase transitions are missing in the simulated dU_n/dx. This arises from the modeling assumption that only a single phase exists in the $0.1 \leq x \leq 0.25$ range (see [21]), which means that contributions from metastable phases (1L and XL–2L) are not considered. Furthermore, the initial potential drop is smaller in the simulation data and exhibits a larger C-rate dependency compared to the experimental data (see Fig. D.6). This difference could arise from the assumption that the distribution width parameter ν is constant in the simulation model (see SI of [21]). However, this assumption may not hold in general as ν, which represents the thermal diffusivity of the system, depends on the temperature and can further depend on the concentration and chemical potential of the electrode [9]. Note also that the simulation model parameters are fitted to different cells than those used for the experimental measurements in this study. This means that the true width parameter of the experimental cell may differ from the simulation cell due to manufacturing-induced variations, which may also explain why the initial dU_n/dx profile is significantly steeper in the experimental data.

After the low SOC region, the dU_n/dx profiles match well, which implies that the simulation model accurately captures the dynamics of the negative electrode for this range. Similarly, the simulated phase evolution (found by Eq. (3)) is plotted together with the experimentally estimated phase evolution in Fig. 12(d–f). For all included currents, the estimated phase evolution approximately equals the simulated phase evolution above 35% SOC. Since dU_n/dx also matches between simulation and experiment for the same range, and since the simulation model is fitted to similar graphite electrodes used in our experiments (see SI of [21]), this suggests that our phase estimation method is capable of accurately inferring the phase content of the negative electrode for mid- to high-range SOC. Note also that lithium plating is only probable in the upper SOC range of our tested currents, where a high degree of Phase 1 content is present in the electrode. Thus, it is less important to accurately estimate the phase content at low SOC, if rapid LIB degradation is to be prevented.

5. Conclusions

In this work, we have demonstrated how kernel smoothing can be used to estimate the phase evolution of graphite electrodes during CC charging. Our findings indicate that the knee-points of the IC curve align well with the knee-points of the electrode phase evolution, and these knee-points could thus be utilized to estimate the phase evolution for low current conditions. At higher currents, it was found that the phase evolution and differential electrode potential are smoothed similarly because of increased phase inhomogeneity in the material. This observation was utilized to fit a logit-normal KDF to smooth the phase estimation found through ICA, which yielded a high estimation accuracy compared with simulations of the phase content with an MAE below 1%pt. per phase. The method was also shown to be accurate above 35% SOC when applied to low-current coin cell measurements, demonstrating its potential as a first step towards BMS-compatible phase tracking. Future work would be to extend this method to varying current scenarios and to validate the estimation results at higher currents. For this to be possible, the reaction-limited model should be extended to a multiple particle model with electrolyte diffusion, and the effects of cell temperature should be considered. Furthermore, the effect of cell aging on the fitting parameter σ_R should be investigated, since this may also lead to a smoothing of the electrode potential.

CRediT authorship contribution statement

Isac Borghed: Writing – review & editing, Writing – original draft, Visualization, Validation, Software, Methodology, Investigation, Formal analysis, Data curation, Conceptualization. **Xiaolei Bian:** Writing – review & editing, Supervision, Software, Methodology, Investigation, Data curation, Conceptualization. **Yicun Huang:** Software, Investigation, Data curation, Writing – review & editing. **Torsten Wik:** Writing – review & editing, Supervision, Resources, Project administration, Funding acquisition, Conceptualization.

Declaration of generative AI and AI-assisted technologies in the writing process

During the preparation of this work the authors used M365 Copilot to assist with language polishing. After using this service, the authors reviewed and edited the content as needed and take full responsibility for the content of the published article.

Declaration of competing interest

The authors declare that they have no known competing financial interests or personal relationships that could have appeared to influence the work reported in this paper.

Acknowledgements

This work was funded by the Swedish Energy Agency under project No. P2023-00144, and the Chalmers Foundation through the Energy Area of Advance. The authors thank Prof. Changfu Zou for valuable discussions during the initial part of the project.

Appendix A. Sensitivity analysis

A.1. SOC estimation

In Section 2.4 we define how the electrode SOC is estimated using Coulomb-counting and an affine mapping to align the Coulomb-SOC with graphite phase transitions described in [22]. The performed SOC transformations are illustrated for experimental data in Fig. A.1: in

Fig. A.1(a) the linear transformation of the Coulomb-SOC using Eq. (4) is shown for the reference measurement (C/40); and in Fig. A.1(b) the transformation is shown for a target measurement (C/5), where a shift using DTW is applied in addition to the linear mapping.

The DTW shift is performed to align the initial charging period of the target measurements with the reference measurement, as each charging cycle starts from approximately the same SOC due to the C/100 CV cutoff current. If such alignment is not performed, any displacement in SOC will influence the fitted σ_t, which introduces additional errors in the estimated phase content. This sensitivity of the phase estimation to misalignment in SOC is illustrated in Fig. A.2, where the phase estimation results are compared for increasing positive and negative displacements from the estimated target SOC. The phase estimation results are shown to be most sensitive at low SOC, where dU_n/dx has the largest magnitude, meaning that small changes in x_T produce large shifts in y_T. This, in turn, significantly affects the cost function in Problem (P). Outside of the initial charging portion ($x > 0.15$), the phase estimation results are less sensitive for the tested alignment errors, but the estimated phase evolution is still smoothed to a larger extent for the greatest alignment errors ($\pm 5\Delta x$). This indicates that the misalignment in SOC results in a higher fitted σ_t.

As can be seen in Fig. A.2(a), there is still a residual misalignment in SOC after the application of the DTW shift, since the reference (x_R, y_R) doesn't perfectly overlap with the target (x_T, y_T). The residual alignment errors are summarized in Table A.1, which shows that the misalignment remains small ($< \Delta x$) for all measurements, indicating that the impact on the phase estimation results is minor, especially outside the low-SOC range (as can be seen in Fig. A.2(b)). The residual alignment error at low SOC may be caused by a limitation of the DTW shift in that it only shifts x_T in integer steps of the sampling distance. Note that at the higher currents (C/2 and 1C), electrolyte dynamics can no longer be neglected, which introduces additional peak displacements at higher SOC. This is discussed further in Section 4.1.2.

In Fig. A.3 the transformation from simulated SOC to experimental SOC using the linear mapping $x = A^{\text{sim}} x^{\text{sim}} + B^{\text{sim}}$ is shown for the reference simulation.

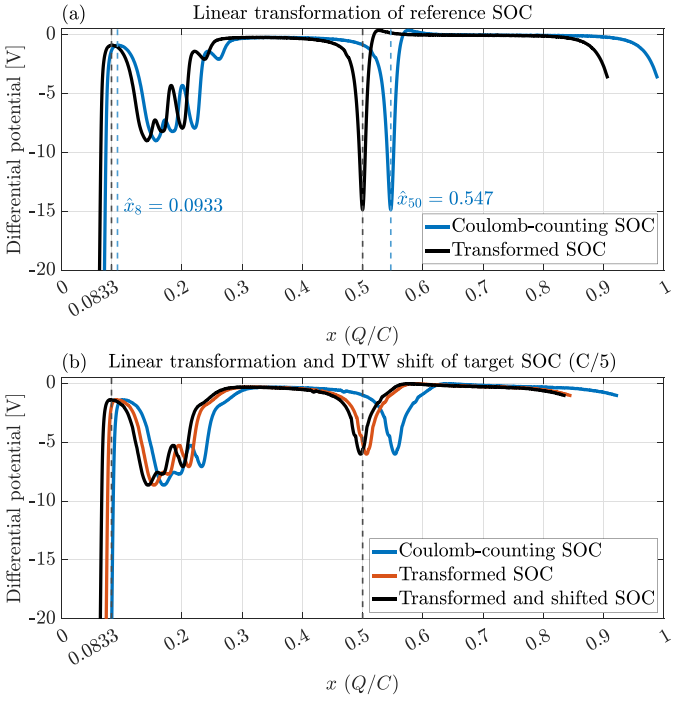

Fig. A.1. Illustrations of the SOC-adjustments used to align Coulomb-counting SOC to graphite phase transitions described in [22], shown for the reference (C/40) measurement in **(a)** and for the C/5 target measurement in **(b)**.

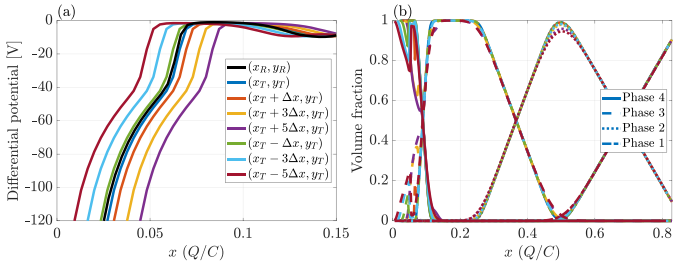

Fig. A.2. Sensitivity of phase estimation for C/5 coin cell measurements with respect to alignment of the target SOC to the reference. In **(a)**, the reference measurement (C/40) is shown together with the target measurement with different levels of displacement in SOC (in terms of the discretization step size $\Delta x \approx 0.003$). The measurements are shown for the interval $x \in [0, 0.15]$, where the phase estimation is particularly sensitive to SOC displacement due to rapid changes in dU_n/dx. In **(b)**, the estimated phase evolution is shown for the different cases of SOC displacement (indicated by the line colors), and where the phases are differentiated by line styles. (For interpretation of the references to color in this figure legend, the reader is referred to the web version of this article.)

Table A.1
Residual alignment errors After applying the DTW shift, measured as the average deviation in x of the target measurements (x_T, y_T) from reference measurements (x_R, y_R) for $x < 0.075$, i.e., before the first peak in dU_n/dx. Note that $\Delta x \approx 0.003$ is the discretization step size.

C-rate	C/20	C/10	C/5	C/2	1C
Misalignment [Δx]	0.21	0.26	0.49	0.28	0.56

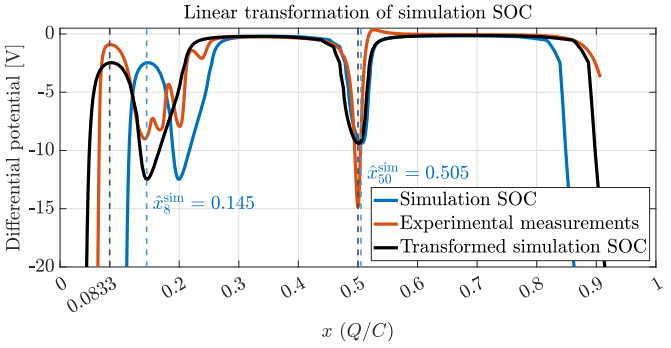

Fig. A.3. Illustration of the linear SOC-transformation used to enable comparison of experimental and simulated data, shown for the C/40 measurement (after the transformation in Fig. A.1(a)) and the C/40 simulation.

A.2. Forgetting factor

In Section 3.2 it was mentioned that λ_k should be selected to be large to "convexify" the optimization problem. This is illustrated in Fig. A.4, where the cost profile is shown for a low value of λ_k ($\lambda_{\max} = 0.2$) and a high value of λ_k ($\lambda_{\max} = 0.99$). Note that the forgetting factor is still variable (in the higher $\lambda_{\max}$ case), according to $\lambda_k = \min(\lambda_{\max}, 0.2 \cdot 1.1^{100 x_T(k)}, 0.2 \cdot 1.1^{100(1-x_T(k))})$. From the figure, it can be seen that the lower forgetting factor produces a cost profile with larger variations, both in x and σ_t, including nonconvexities in σ_t. This contrasts with the high λ_k case, where the cost profile changes slowly with x and convexity in σ_t is achieved.

Furthermore, the forgetting factor also influences the noise sensitivity of the phase estimation results. The phase estimation results for simulated C/20 lithiation are compared for four noise levels: noise free (the same results as Fig. D.1(a)), low noise (additive zero-mean, white Gaussian noise with standard deviation of 0.03 mV), moderate noise

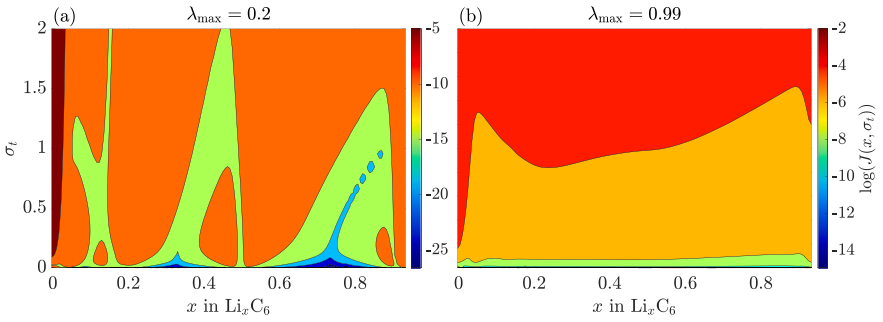

Fig. A.4. Logarithmic cost function profile for different maximum forgetting factors for simulated C/20 lithiation (i.e., the measurements shown in Fig. D.1(a)), $\lambda_{\max} = 0.2$ **(a)** and $\lambda_{\max} = 0.99$ **(b)**. Here $J(x, \sigma_t)$ is the cost function which is minimized in Problem (P). Several regions with nonconvexity in σ_t are found for the low-λ case.

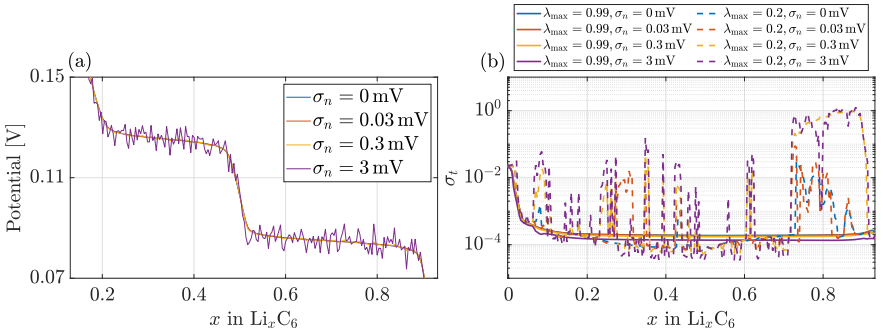

Fig. A.5. Simulated C/20 lithiation (i.e., the measurements shown in Fig. D.1(a)) with additive Gaussian noise with different standard deviations σ_n **(a)** and noise sensitivity of fitted σ_t for different values of $\lambda_{\max}$ **(b)**.

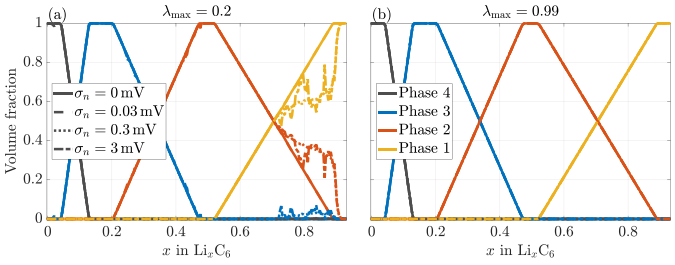

Fig. A.6. Phase estimation sensitivity to noise for simulated C/20 lithiation with additive Gaussian noise (i.e., the measurements shown in Fig. A.5(a)) for different maximum forgetting factors: $\lambda_{\max} = 0.2$ **(a)** and $\lambda_{\max} = 0.99$ **(b)**. In both subfigures, the noise levels are differentiated by line style, and the phases are differentiated by color. (For interpretation of the references to color in this figure legend, the reader is referred to the web version of this article.)

(standard deviation 0.3 mV), and high noise (standard deviation 3 mV). The low noise case is representative of the PAT-Cell-Force used for experimental coin cell measurements, as voltage measurements with the PAT-Channel have a specified upper bound on noise of $30\,\mu$ V [34]. The different noise cases are shown in Fig. A.5, together with the resulting values of σ_t for the two cases of $\lambda_{\max}$ (0.2 and 0.99). From the figure it can be observed that the noise has a large effect on the fitted σ_t when the forgetting factor is low, while the high forgetting factor results in a relatively constant σ_t for the different noise levels. The phase estimation results for these values of σ_t are shown in Fig. A.6, where the low forgetting factor case exhibits a high sensitivity to noise (due to the dependence of σ_t on the noise level), while the high forgetting factor case displays no visible impact on the phase estimation performance due to noise.

Appendix B. Kernel density function

During initial testing, a truncated Gaussian distribution was used as KDF, instead of the logit-normal distribution. This distribution has the probability density function (PDF)

$$f^{\text{Gauss}}_{\mu,\sigma}(x_R) = \frac{\phi_{\mu,\sigma}(x_R)}{Z^{\text{Gauss}}(\mu,\sigma)}, \tag{B.1}$$

where $\phi_{\mu,\sigma}$ is the PDF of a Gaussian distribution with mean μ and standard deviation σ, and $Z^{\text{Gauss}} = \Phi_{\mu,\sigma}(\max(\mathbb{X}_R)) - \Phi_{\mu,\sigma}(\min(\mathbb{X}_R))$ is a normalization factor calculated from the Gaussian CDF, $\Phi_{\mu,\sigma}$. Fitted logit-normal KDFs and truncated Gaussian KDFs are shown for the 1C lithiation experiment in Fig. B.1, together with fitted beta distributions [29]:

$$f^{\text{Beta}}_{\alpha,\beta}(x_R) = \frac{1}{\text{Beta}(\alpha,\beta)} x_R^{\alpha-1}(1-x_R)^{\beta-1}\frac{1}{Z^{\text{Beta}}(\alpha,\beta)}, \tag{B.2}$$

where $\text{Beta}(\alpha,\beta) = \Gamma(\alpha)\Gamma(\beta)/\Gamma(\alpha+\beta)$ is the beta function and $Z^{\text{Beta}}(\alpha,\beta)$ is a normalization constant calculated from the beta CDF function over the interval $\mathbb{X}_R$ so that $f^{\text{Beta}}_{\alpha,\beta}(x_R)$ represents a PDF. To reduce the number of fitting parameters, the beta distribution is re-parametrized with respect to a specified mean of the distribution (set equal to the SOC, x_T), using the relation

$$x_T = \text{mean}(\alpha,\beta) = \frac{\alpha}{\alpha+\beta} \leftrightarrow \beta = \frac{1-x_T}{x_T}\alpha. \tag{B.3}$$

With this formulation, the beta distribution is determined by one unknown parameter, α, which simplifies the fitting problem. Note, however, that the fitting problem suffers from numerical issues due to the

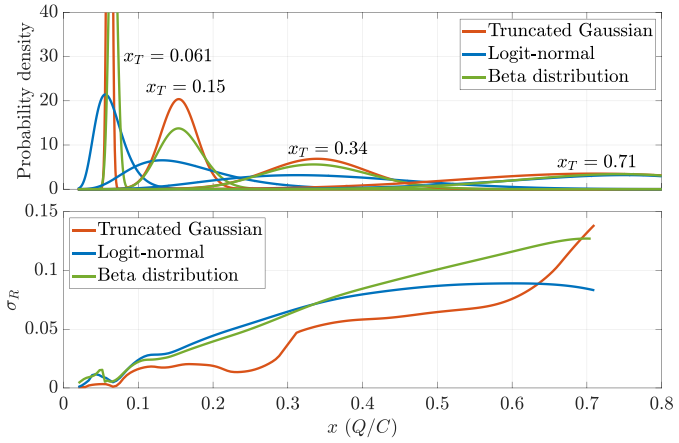

Fig. B.1. Comparison of fitted logit-normal, truncated Gaussian, and beta KDFs for the 1C lithiation of a coin cell, plotted together with the resulting standard deviation σ_R in the lower figure. The distributions are shown at four different states of charge, Given by the annotations.

fact that the beta function must be evaluated for large values of α and β. For example, the fitted value of α at $x_T \approx 0.066$ in the 1C measurement is $\alpha \approx 144.1$, resulting in a corresponding $\beta \approx 2025.7$. Inserting these values into the beta function gives $\text{Beta}(\alpha, \beta) \approx 1.596 \times 10^{-231}$, for which the division in Eq. (B.2) risks large losses of precision.

In Fig. B.1, it is noted that the fitted truncated Gaussian KDFs are always symmetric, while the logit-normal and beta KDFs become skewed close to the SOC edges. Furthermore, the logit-normal distribution changes less drastically over the SOC interval compared to both the beta and truncated Gaussian distributions, and the logit-normal KDF is the only distribution where the fitted standard deviation starts decreasing at high SOC.

Appendix C. Result metrics

In the simulation results, the mean absolute phase estimation error is used to evaluate the phase prediction accuracy; it is defined as

$$\text{MAE}(\hat{p}) = \frac{100}{n} \sum_{t=1}^{n} \sum_{i=1}^{4} |p_i(t) - \hat{p}_i(t)| \quad [\%\text{pt.}], \tag{C.1}$$

where $\hat{p}_i(t)$ is the predicted value and $p_i(t)$ is the true volume fraction of Phase i at time t. The phase estimation error is measured in percentage points, reflected by the scaling with 100.

The MAE is also used to measure the fitting accuracy of the smoothed reference signal $\mathbb{E}_{f_{\mu,\sigma}}[y_R]$ to the target measurements y_T according to

$$\text{MAE}(y_T) = \frac{1}{n\bar{y}_R} \sum_{t=1}^{n} \sqrt{e^2(t; \text{logit}(x_T(t)), \sigma_t^*)}, \tag{C.2}$$

where $e^2(t; \text{logit}(x_T(t)), \sigma_t^*)$ is the squared fitting error, defined in Eq. (10), and $\bar{y}_R$ is the arithmetic mean of the reference measurement time series $y_R(t)$. The normalization with $\bar{y}_R$ is introduced to enable comparison between the potential and differential potential fitting accuracies, as those signals differ notably in magnitude (see for instance Fig. D.1(a, b)).

Appendix D. Additional results

The phase estimation and kernel fitting results for simulated C/20 and C/10 lithiation of a graphite half-cell are found in Figs. D.1 and D.2, respectively. For these currents the phase estimation performance is similar for both the potential and differential potential signals, in contrast to C/5 lithiation where the differential potential yielded better estimation results (see Fig. 7). For the same currents, the phase estimation results using experimental differential potential measurements are presented in Fig. D.3.

Additional phases were present in the experimental data compared to simulation. In Figs. 10 and D.3 the additional phases were combined to allow comparison with the simulated half-cell data, whereas in Fig. D.4 the estimated phase evolution for all phases identified from the peaks of the dU_n/dx profile is shown.

In the experimental results summarized in Table 5, it was mentioned that the first sample was excluded before calculating the MAE for the C/20 and C/5 measurements. This was done because the fitting error for the first sample was significantly higher for these two measurements, and since the magnitude of dU_n/dx is drastically larger for low SOC (see Fig. D.5), this would introduce a bias in the fitting MAE unless these two measurements are discarded.

In Fig. 12(a) the experimental and simulated dU/dx profiles are compared over the full SOC range, but the y-axis in the figure has been limited to facilitate comparison for $x > 0.05$. This was done since dU/dx is significantly lower in the initial charging period; for this range a separate comparison is found in Fig. D.6.

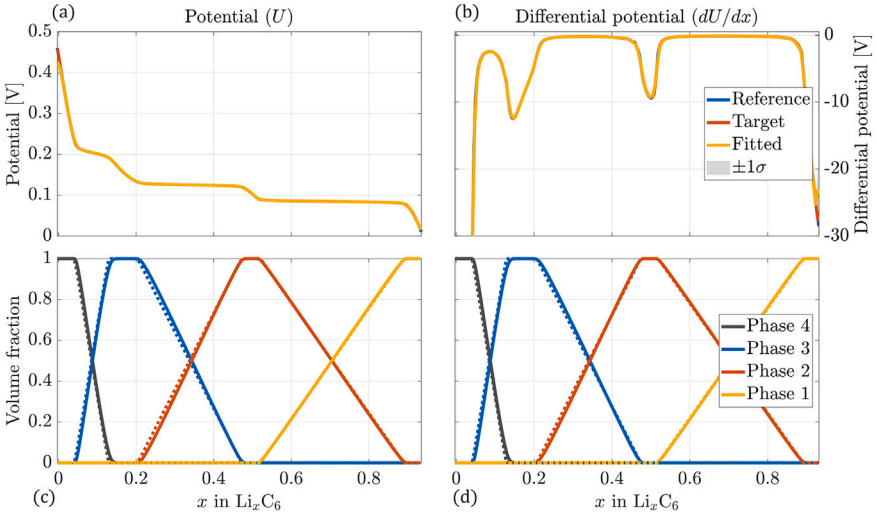

Fig. D.1. Fitting and phase estimation results for simulated C/20 lithiation of a graphite half-cell. In **(a,c)** the electrode potential is used to fit the KDF, and in **(b,d)** the differential potential (dU/dx) is used. C/40 was used as reference for all cases. In **(c,d)** the solid lines represent the ground truth phase evolution while the dotted lines represent the estimated phase evolution.

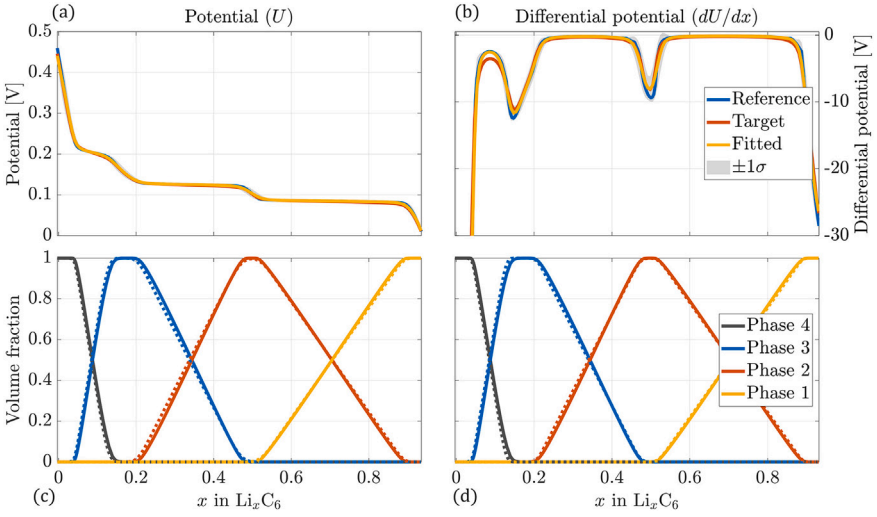

Fig. D.2. Fitting and phase estimation results for simulated C/10 lithiation of a graphite half-cell. In **(a,c)** the electrode potential is used to fit the KDF, and in **(b,d)** the differential potential (dU/dx) is used. C/40 was used as reference for all cases. In **(c,d)** the solid lines represent the ground truth phase evolution while the dotted lines represent the estimated phase evolution.

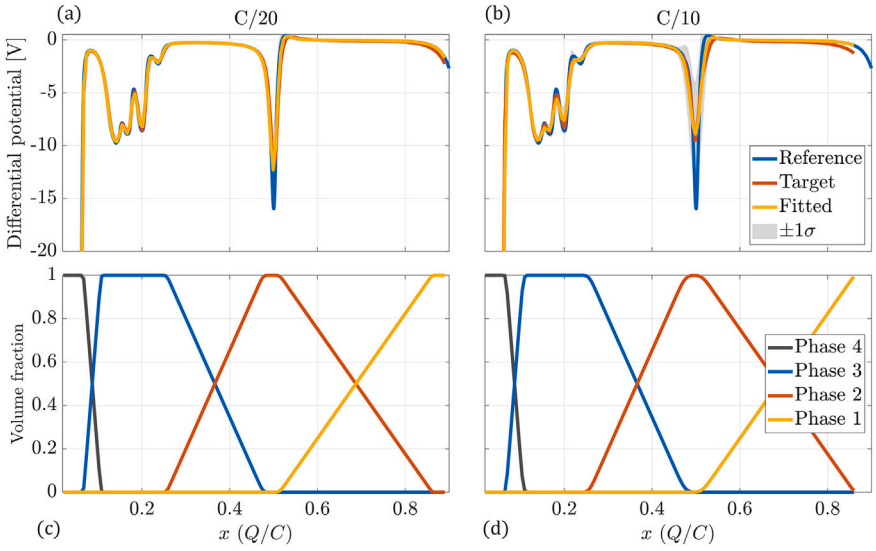

Fig. D.3. Fitting and phase estimation results from experimental differential negative electrode potential (dU_n/dx) measurements during C/20 **(a,c)** and C/10 **(b,d)** lithiation of a coin cell (using C/40 as reference).

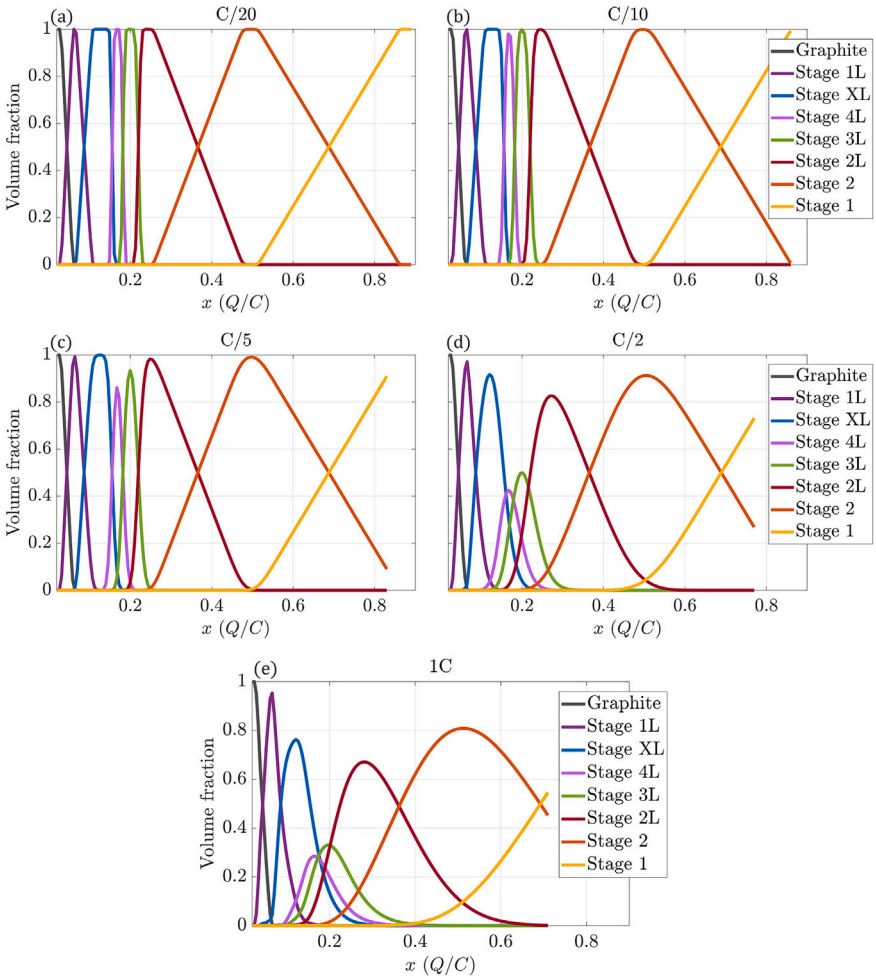

Fig. D.4. Estimation results of all stages from experimental differential potential (dU_n/dx) measurements during C/20 **(a)**, C/10 **(b)**, C/5 **(c)**, C/2 **(d)**, and 1C **(e)** lithiation of a coin cell (using C/40 as reference).

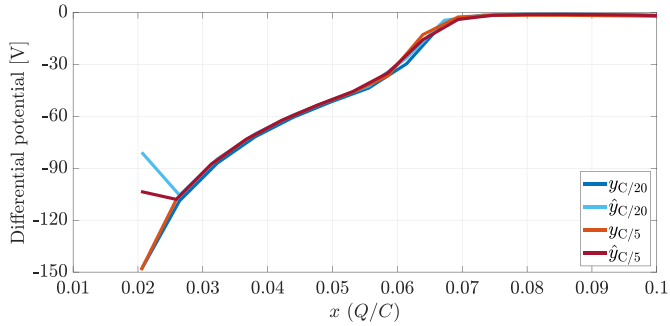

Fig. D.5. Differential potential measurements, y_T, and smoothing fit $\hat{y}_T = \mathbb{E}_{f_{\mu,\sigma}}[y_R]$, for the C/20 and C/5 measurements at low SOC. Since the initial magnitudes of y_T are large, the initial estimation error $|\hat{y}_T - y_t|$ is excluded from the calculation of the Fitting MAE to avoid biasing the metric towards the low-SOC range.

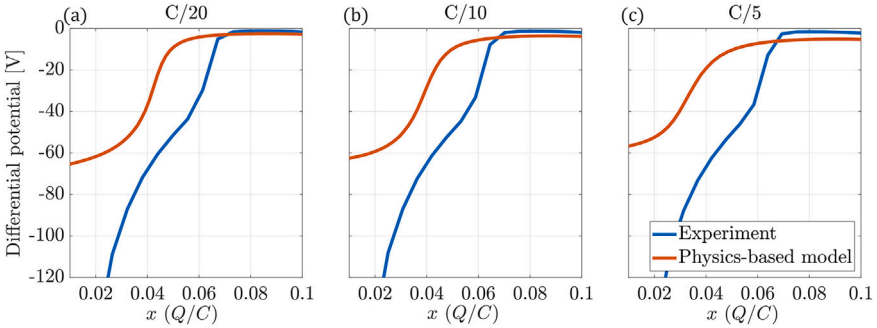

Fig. D.6. Comparison of simulated differential half-cell potential (red) and experimentally measured differential negative electrode potential (blue) for C-rates **(a)** C/20, **(b)** C/10, and **(c)** C/5 at low SOC ($x < 0.1$). (For interpretation of the references to color in this figure legend, the reader is referred to the web version of this article.)

Data availability

Data will be made available on request.

References

[1] M. Hasan, R. Haque, M. Jahirul, M. Rasul, I. Fattah, N. Hassan, M. Mojifur, Advancing energy storage: the future trajectory of lithium-ion battery technologies, J. Energy Storage 120 (2025) 116511, https://doi.org/10.1016/j.est.2025.116511

[2] B. Bose, A. Garg, B.K. Panigrahi, J. Kim, Study on Li-ion battery fast charging strategies: review, challenges and proposed charging framework, J. Energy Storage 55 (2022) 105507, https://doi.org/10.1016/j.est.2022.105507

[3] X. Han, L. Lu, Y. Zheng, X. Feng, Z. Li, J. Li, M. Ouyang, A review on the key issues of the lithium ion battery degradation among the whole life cycle, eTransp. 1 (2019) 100005, https://doi.org/10.1016/j.etran.2019.100005

[4] J. Leijon, Charging strategies and battery ageing for electric vehicles: a review, Energy Strategy Rev. 57 (2025) 101641, https://doi.org/10.1016/j.esr.2025.101641

[5] X. Lin, K. Khosravinia, X. Hu, J. Li, W. Lu, Lithium plating mechanism, detection, and mitigation in lithium-ion batteries, Progr. Energy Combust. Sci. 87 (2021) 100953, https://doi.org/10.1016/j.pecs.2021.100953

[6] J. Wang, Y. Gao, J. Liu, H. Liao, L. Wang, X. He, Operando X-Ray diffraction boosting understanding of graphite phase evolution in lithium-ion batteries, Small Methods 8 (3) (2024) 2301084, https://doi.org/10.1002/smtd.202301084

[7] T.R. Ferguson, M.Z. Bazant, Nonequilibrium thermodynamics of porous electrodes, J. Electrochem. Soc. 159 (12) (2012) A1967, https://doi.org/10.1149/2.048212jes

[8] R.B. Smith, M.Z. Bazant, Multiphase porous electrode theory, J. Electrochem. Soc. 164 (11) (2017) E3291, https://doi.org/10.1149/2.0171711jes

[9] H. Zhao, M.Z. Bazant, Population dynamics of driven autocatalytic reactive mixtures, Phys. Rev. E 100 (1) (2019) 012144, https://doi.org/10.1103/PhysRevE.100.012144

[10] H. Lian, M.Z. Bazant, Modeling lithium plating onset on porous graphite electrodes under fast charging with hierarchical multiphase porous electrode theory, J. Electrochem. Soc. 171 (1) (2024) 010526, https://doi.org/10.1149/1945-7111/ad1e3d

[11] A. Raj, I.A. Shkrob, J.S. Okasinski, M.-T. Fonseca Rodrigues, A.C. Chuang, X. Huang, D.P. Abraham, Spatially-resolved lithiation dynamics from *operando* X-ray diffraction and electrochemical modeling of lithium-ion cells, J. Power Sources 484 (2021) 229247, https://doi.org/10.1016/j.jpowsour.2020.229247

[12] C. Schmitt, A. Kube, N. Wagner, K.A. Friedrich, Understanding the influence of temperature on phase evolution during lithium-graphite (de-)intercalation processes: an operando X-ray diffraction study, Chemelectrochem 9 (2) (2022) e202101342, https://doi.org/10.1002/celc.202101342

[13] C. Weisenberger, D.K. Harrison, C. Zhou, V. Knoblauch, Revealing the effects of microstructural changes of graphite anodes during cycling on their lithium intercalation kinetics utilizing operando XRD, Electrochim. Acta 461 (2023) 142629, https://doi.org/10.1016/j.electacta.2023.142629

[14] A. Olgo, S. Genies, R. Franchi, C. Septet, Q. Jacquet, Q. Berrod, R. Palm, P. Chenevier, E. Villemin, C. Villevieille, N. Blanc, S. Tardif, O. Raccurt, S. Lyonnard, Revealing how internal sensors in a smart battery impact the local graphite lithiation mechanism, Nat. Commun. 15 (1) (2024) 10258, https://doi.org/10.1038/s41467-024-54656-6

[15] I.A. Bobrikov, N.Y. Samoylova, S.V. Sumnikov, O.Y. Ivanshina, R.N. Vasin, A.I. Beskrovnyi, A.M. Balagurov, *in-situ* time-of-flight neutron diffraction study of the structure evolution of electrode materials in a commercial battery with $LiNi_{0.8}Co_{0.15}Al_{0.05}O_2$ cathode, J. Power Sources 372 (2017) 74–81, https://doi.org/10.1016/j.jpowsour.2017.10.052

[16] C. Didier, W.K. Pang, Z. Guo, S. Schmid, V.K. Peterson, Phase evolution and intermittent disorder in electrochemically lithiated graphite determined using in operando neutron diffraction, Chem. Mater. 32 (6) (2020) 2518–2531, https://doi.org/10.1021/acs.chemmater.9b05145

[17] B. Zheng, X. Liu, Y. Xiang, Solid-state nuclear magnetic resonance studies of lithium and sodium metal batteries, J. Phys. Chem. C 128 (44) (2024) 18659–18677, https://doi.org/10.1021/acs.jpcc.4c05822

[18] A.P. Black, C. Escudero, F. Fauth, M. Fehse, G. Agostini, M. Reynaud, R.G. Houdeville, D. Chatzogiannakis, J. Orive, A. Ramo-Irurre, M. Casas-Cabanas, M.R. Palacin, Beam effects in synchrotron radiation operando characterization of battery materials: X-Ray diffraction and absorption study of $LiNi_{0.33}Mn_{0.33}Co_{0.33}O_2$ and $LiFePO_4$ electrodes, Chem. Mater. 36 (11) (2024) 5596–5610, https://doi.org/10.1021/acs.chemmater.4c00597

[19] M. Dubarry, B.Y. Liaw, M.-S. Chen, S.-S. Chyan, K.-C. Han, W.-T. Sie, S.-H. Wu, Identifying battery aging mechanisms in large format li ion cells, J. Power Sources 196 (7) (2011) 3420–3425, https://doi.org/10.1016/j.jpowsour.2010.07.029

[20] A. Fly, R. Chen, Rate dependency of incremental capacity analysis (dQ/dV) as a diagnostic tool for lithium-ion batteries, J. Energy Storage 29 (2020) 101329, https://doi.org/10.1016/j.est.2020.101329

[21] Y. Huang, Q. Zhu, T. Wik, D.P. Finegan, Y. Li, C. Zou, BMINN: learning chemical potentials and parameters from voltage data for multi-phase battery modeling, Energy Storage Mater. 86 (2026) 104997, https://doi.org/10.1016/j.ensm.2026.104997

[22] H. Fujimoto, T. Yamaki, K. Shimoda, S. Fujinami, T. Nakatani, G. Kano, M. Kawasaki, Z. Ogumi, T. Abe, Phase diagram of Li-Graphite intercalation compound formed by the Charge/Discharge reaction in Li-ion battery, J. Electrochem. Soc. 169 (7) (2022) 070507, https://doi.org/10.1149/1945-7111/ac7e77

[23] S. Schweidler, L. de Biasi, A. Schiele, P. Hartmann, T. Brezesinski, J. Janek, Volume changes of graphite anodes revisited: a combined operando X-ray diffraction and in situ pressure analysis study, J. Phys. Chem. C 122 (16) (2018) 8829–8835, https://doi.org/10.1021/acs.jpcc.8b01873
[24] D. Sheptyakov, L. Boulet-Roblin, V. Pomjakushin, P. Borel, C. Tessier, C. Villevieille, Stroboscopic neutron diffraction applied to fast time-resolved operando studies on Li-ion batteries (d-$LiNi_{0.5}Mn_{1.5}O_4$ vs. graphite), J. Mater. Chem. A 8 (3) (2020) 1288–1297, https://doi.org/10.1039/C9TA11826H
[25] MathWorks Inc, MATLAB documentation: DTW function, 2025, https://se.mathworks.com/help/signal/ref/dtw.html (Accessed 4 August 2025).
[26] R.W. Schafer, What *Is* a Savitzky-Golay filter? [Lecture notes], IEEE Signal Process. Mag. 28 (4) (2011) 111–117, https://doi.org/10.1109/MSP.2011.941097
[27] MathWorks Inc, MATLAB documentation: findpeaks function, 2025, https://se.mathworks.com/help/signal/ref/findpeaks.html (Accessed 30 June 2025).
[28] J. Aitchison, S.M. Shen, Logistic-normal distributions: some properties and uses, Biometrika 67 (2) (1980) 261–272, https://doi.org/10.2307/2335470
[29] M. Bourguignon, D.I. Gallardo, A general and unified parameterization of the beta distribution: a flexible and robust beta regression model, Stat. Neerl. 79 (2) (2025) e70007, https://doi.org/10.1111/stan.70007
[30] K.G. Gallagher, D.W. Dees, A.N. Jansen, D.P. Abraham, S.-H. Kang, A volume averaged approach to the numerical modeling of phase-transition intercalation electrodes presented for Li_xC_6, J. Electrochem. Soc. 159 (12) (2012) A2029, https://doi.org/10.1149/2.015301jes
[31] D.W. Bacon, D.G. Watts, Estimating the transition between two intersecting straight lines, Biometrika 58 (3) (1971) 525–534, https://doi.org/10.1093/biomet/58.3.525
[32] MathWorks Inc, MATLAB documentation: fminsearch function, 2025, https://se.mathworks.com/help/matlab/ref/fminsearch.html (Accessed 30 June 2025).
[33] F.Y. Kuo, D. Nuyens, Application of quasi-Monte Carlo methods to elliptic PDEs with random diffusion coefficients: a survey of analysis and implementation, Found. Comput. Math. 16 (2016) 1631–1696, https://doi.org/10.1007/s10208-016-9329-5
[34] El-Cell GmbH, User manual: PAT-Channel-1, 2024, https://www.el-cell.com/products/pat-battery-tester/pat-tester-x/pat-channel-1/#1600689049692-348ecaad-f597 (Accessed 8 April 2026).